



# CHORUS

This is the accepted manuscript made available via CHORUS. The article has been published as:

## Microwave ac Zeeman force for ultracold atoms

C. T. Fancher, A. J. Pyle, A. P. Rotunno, and S. Aubin

Phys. Rev. A **97**, 043430 — Published 27 April 2018

DOI: [10.1103/PhysRevA.97.043430](https://doi.org/10.1103/PhysRevA.97.043430)

# Microwave AC Zeeman Force for Ultracold Atoms

C. T. Fancher\*, A. J. Pyle, A. P. Rotunno, and S. Aubin  
*Dept. of Physics, College of William and Mary, Williamsburg, VA 23187\**  
 (Dated: March 19, 2018)

We measure the AC Zeeman force on an ultracold gas of  $^{87}\text{Rb}$  due to a microwave magnetic field targeted to the 6.8 GHz hyperfine splitting of these atoms. An atom chip produces a microwave near-field with a strong amplitude gradient, and we observe a force over three times the strength of gravity. Our measurements are consistent with a simple 2-level theory for the AC Zeeman effect and demonstrate its resonant, bipolar, and spin-dependent nature. We observe that the dressed atom eigenstates gradually mix over time and have mapped out this behavior as a function of magnetic field and detuning. We demonstrate the practical spin-selectivity of the force by pushing or pulling a specific spin state while leaving other spin states unmoved.

**PACS numbers:** May be entered using the `\pacs{#1}` command.

## I. INTRODUCTION

Atomic physics has developed a formidable toolbox of experimental techniques for precision control of the external and internal states of atoms. The quantum control of internal states has led to the development of Ramsey interferometry [1], atomic clocks [2–4], and spin polarized gases [5, 6], among other applications. The precision control of the external degrees of freedom using laser cooling, evaporative cooling, and optical and magnetic traps are the key techniques for producing ultracold quantum gases [7, 8]. Notably however, methods that couple internal and external control remain more challenging and less versatile: optical Raman pulses can selectively kick a given spin state, but cannot trap it. A DC magnetic field produces spin-dependent potentials for each spin state, but these are all proportional. Optical dipole potentials at a magic wavelength behave similarly or must be periodic [9–11].

The AC Zeeman (ACZ) effect can be used to produce fully spin-dependent potentials and is a versatile addition to the quantum control toolbox [12–14]. In principle, multiple spin states can be selectively targeted with qualitatively different and independent potentials simultaneously. ACZ forces are broadly applicable to atomic systems with non-degenerate spin states. The ACZ force is resonant and bipolar, such that any hyperfine state can be either a weak- or strong-field seeker [15]. In the case of alkali hyperfine ground states, the relevant transitions are in the microwave ( $\mu\text{w}$ ) and so are essentially immune to spontaneous emission.

However, since first being proposed and implemented for atomic beam [12, 13] and cold atom systems [15, 16], ACZ potentials have seen only occasional use due to the limitations of propagating (far-field)  $\mu\text{w}$  fields. The length scale for intensity variations in the far-field is given by the wavelength (cm-scale or larger), which severely limits the gradients and ACZ forces that are feasible at

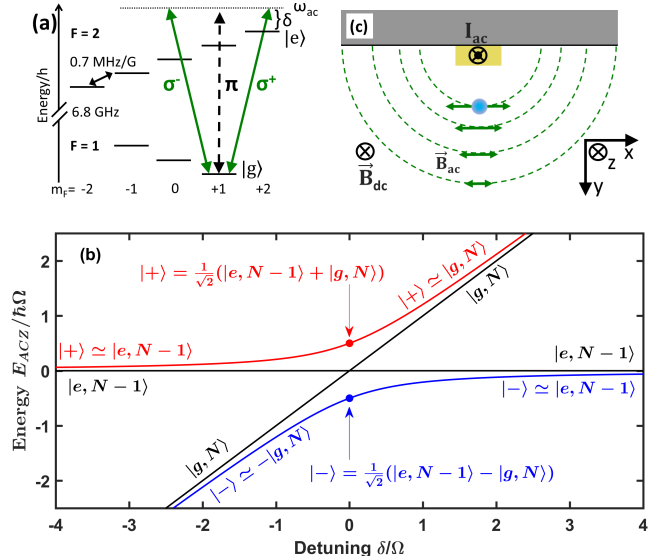


FIG. 1. Experimental scheme. (a) Hyperfine ground levels of  $^{87}\text{Rb}$  ( $5S_{1/2}$ ) and relevant transitions (green). (b) Plot of the eigenenergies  $E_{ACZ}$  (red and blue avoided crossing curves) for the  $|\pm\rangle$  eigenstates versus  $\mu\text{w}$  detuning  $\delta$ , along with the energies of the dressed atom basis states (black). (c) Atom chip set-up. An ODT confines atoms (blue dot) a distance  $d \approx 100 \mu\text{m}$  below a  $z$ -axis wire (yellow), which supports a 6.8 GHz current  $I_{ac}$  that generates the  $\mu\text{w}$  magnetic near-field  $\vec{B}_{ac}$ .

practical  $\mu\text{w}$  powers. For example, the ACZ potential produced by a  $\mu\text{w}$  power build-up cavity in ref. 16 was sufficient for weak horizontal confinement of cold atoms, but could not hold these against gravity.

More recently, strong ACZ forces have become feasible with atom chip-based  $\mu\text{w}$  near-fields, in which the length scale for field variations is set by the geometry of the  $\mu\text{w}$  currents. This technology change has enabled the use of ACZ potentials for spin-dependent interferometry [17], spin-squeezing, and ion-based quantum gates [18, 19]. However, despite these recent applications, the ACZ effect has not been studied experimentally on its own. We note that ACZ potentials are distinct from

\* Present Address: Naval Research Laboratory, Washington, D.C. 20375

adiabatic RF potentials [20], though both effects can be present simultaneously. ACZ potentials use a uniform DC magnetic field and produce a force with an AC field gradient. Adiabatic RF potentials produce a force with a DC magnetic gradient and use an AC field to couple DC high field-seeking and DC low field-seeking spin states.

We describe our experimental system (section II) and present the first detailed measurements of the ACZ force in an ultracold gas of neutral  $^{87}\text{Rb}$  atom and find reasonable agreement with 2-level dressed atom theory (section III). We study the time-evolution of a  $\mu\text{w}$ -dressed spin state as a function of magnetic field and detuning (section IV). Finally, we use the ACZ force to push, pull, and remove a specific spin state within a spin mixture (section V).

## II. EXPERIMENTAL SYSTEM

In the  $5S_{1/2}$  ground levels of  $^{87}\text{Rb}$  (see Fig. 1(a)), the  $|e\rangle = |F = 2, m_F = 2\rangle$  and  $|g\rangle = |1, 1\rangle$  hyperfine states form an effective 2-level system with transition energy  $\hbar\omega_0$ . When driven by a  $\mu\text{w}$  magnetic field  $B_{ac}$  at frequency  $\omega_{ac}$  and detuning  $\delta = \omega_{ac} - \omega_0$ , atoms in  $|e\rangle$  can only transition to  $|g\rangle$  directly. Atoms in  $|g\rangle$  can transition to  $|e\rangle$ ,  $|2, 1\rangle$ , and  $|2, 0\rangle$ , though off-resonant excitation of these last two is suppressed for large energy separations.

Following the original treatment of Agosta et al. [15], we use a dressed-atom basis  $\{|g, N\rangle, |e, N - 1\rangle\}$  to describe an  $N$  photon  $\mu\text{w}$  field and a 2-level atom. Alternatively, an equivalent semi-classical treatment of the  $\mu\text{w}$  field uses the  $\{|g\rangle, |e\rangle\}$  basis of bare atomic states in a rotating frame. As shown in Fig 1(b), the two basis states (black lines) differ in energy by  $\hbar\delta$ , but are degenerate on-resonance. The interaction between the  $\mu\text{w}$  field and the atom produces two energy eigenstates that are linear combinations of the basis states: a weak-field seeking  $|+\rangle$  state and a strong-field seeking  $|-\rangle$  state [15]. Fig. 1(b) shows that once the interaction is included, the on-resonance degeneracy of the basis state energy levels becomes an avoided crossing for the  $|\pm\rangle$  eigenstates (red and blue lines). The system can be made to travel along either eigenenergy curve by an adiabatic rapid passage (ARP) sweep of  $\delta$ . For example,  $|e, N - 1\rangle$  can access the  $|-\rangle$  ( $|+\rangle$ ) eigenstate at any  $\delta$  by sweeping from a large positive (negative) initial detuning.

A spatially varying  $\vec{B}_{ac}(\vec{r})$  results in an ACZ energy [15] gradient and the following ACZ force for  $|\pm\rangle$ :

$$\vec{F}_{ac,|\pm\rangle} = \pm \frac{\hbar}{2} \frac{\Omega}{\sqrt{\delta^2 + \Omega^2}} (-\vec{\nabla}\Omega(\vec{r})) \quad (1)$$

where  $\Omega(\vec{r}) = \langle g | -\vec{\mu} \cdot \vec{B}_{ac}(\vec{r}) | e \rangle / \hbar$  is the Rabi frequency, and  $B_{ac}$  is the amplitude of the AC magnetic field. Neglecting the nuclear spin, the magnetic moment is  $\vec{\mu} = (2\mu_B/\hbar)\vec{S}$ , where  $\mu_B$  is the Bohr magneton, and  $\vec{S}$  is the valence electron spin operator.

A sketch of the experimental set-up and coordinate system are shown in Fig. 1(c). A thermal cloud of  $10^5$  ultracold  $^{87}\text{Rb}$  atoms in  $|e\rangle$  is transferred from an atom chip micro-magnetic trap [21] into an optical dipole trap (ODT) located roughly  $100 \mu\text{m}$  below the chip's surface. The ODT consists of two crossed  $1064 \text{ nm}$  laser beams: a  $1.2 \text{ W}$  beam directed along  $\hat{z}$  with a  $1/e^2$  waist radius of  $60 \mu\text{m}$  and a  $0.8 \text{ W}$  beam along  $\hat{x}$  (with a small  $\hat{y}$  component) with a waist radius of  $120 \mu\text{m}$ . The resulting cigar-shaped ODT has trapping frequencies  $\omega_{(x,y,z)} = 2\pi \times (186, 164, 28) \text{ Hz}$ , a calculated depth of  $23 \mu\text{K}$ , and atoms in  $|e\rangle$  at  $0.32 \mu\text{K}$  with calculated RMS radius  $\sigma_{x,y} \simeq 5 \mu\text{m}$ . A uniform magnetic field  $B_{dc}$  defines the quantization  $z$ -axis for atomic spin states. Gravity is down along  $\hat{y}$ .

We generate the  $\mu\text{w}$  magnetic near-field  $B_{ac}$  by directing  $6.8 \text{ GHz}$  microwaves from a  $3 \text{ W}$  amplifier into a  $z$ -axis wire above the atoms (see Fig. 1(c)). Due to significant losses in the amplifier-to-chip cabling, only a small fraction ( $\sim 15\%$ ) of the  $\mu\text{w}$  power makes it to the chip. Furthermore, we do not impedance match the microwaves to the chip and so suffer additional loss due to reflection. Nevertheless, the generated  $\mu\text{w}$  current  $I_{ac}$  is sufficiently large to produce a significant  $B_{ac}$  and ACZ force. The chip wire into which we direct the  $\mu\text{w}$  power is roughly in the form of a "U": The central segment is along the  $z$ -axis directly above the atoms, as shown in Fig. 1(c), with length  $2 \text{ mm}$ , width  $50 \mu\text{m}$ , and thickness  $3 \mu\text{m}$ . The resulting  $B_{ac}$  is expected to be primarily polarized along  $\hat{x}$  at the atoms and drive  $\sigma^\pm$  transitions ( $\Delta m_F = \pm 1$ ). Stray polarization along  $\hat{z}$  drives  $\pi$  transitions ( $\Delta m_F = 0$ ), as shown in Fig. 1(a). The  $\mu\text{w}$  current distribution in neighboring wires (due to capacitive and inductive coupling) is not known, but its effect on the near-field  $B_{ac}$  at the atoms is included when one measures  $\Omega$  and  $\vec{\nabla}\Omega$ .

## III. AC ZEEMAN FORCE

We measure the ACZ force by turning off the ODT and applying a  $\mu\text{w}$  pulse of duration  $t_{\mu\text{w}} = 0.5 \text{ ms}$ . The resulting ACZ impulse to the atoms is along  $\hat{y}$  ( $\pm 5^\circ$ ). We measure the impulse velocity  $\Delta v = \Delta y / \Delta t$  by absorption imaging of atoms in  $|e\rangle$  for a time of flight  $\Delta t = 12.25 \text{ ms}$ ;  $\Delta y$  is the change in the atoms'  $y$ -position due to the  $\mu\text{w}$  pulse (see Fig. 2(a-b)). As a first approximation, we assume that the cloud size and  $t_{\mu\text{w}}$  are sufficiently small that the ACZ force is constant in space and time over the duration of the pulse. The force is given by  $F_{ac} = m\Delta v / t_{\mu\text{w}}$  with  $m$  as the mass of an atom.

We can apply the  $\mu\text{w}$  pulse with or without an ARP sweep. For the no-ARP case, the  $\mu\text{w}$  pulse is applied directly to atoms in  $|e\rangle$  at a fixed  $\delta$ , and the cloud splits in two (see Fig. 2(a), no-ARP) according to the projection of  $|e\rangle$  onto the  $|+\rangle$  (push-down) and  $|-\rangle$  (pull-up) states. If a brief ARP sweep ( $0.1 \text{ ms}$ ) is added to the start of the  $\mu\text{w}$  pulse, then the atoms are prepared in one of the  $|\pm\rangle$

states, and the entire cloud experiences either a “push” or a “pull”. The ARP sweeps start at a large initial detuning  $\delta_0 = \pm 13$  MHz to populate the  $|\mp\rangle$  state and ends at the  $\mu\text{w}$  pulse detuning  $\delta_{exp}$ . The ARP frequency ramp is sufficiently slow compared to the Rabi frequency ( $|d\delta/dt| \ll |\Omega|$ ) that atoms initially in  $|e\rangle$  travel adiabatically along the  $|+\rangle$  ( $|-\rangle$ ) eigenenergy curve in Fig. 1(b) for an upward (downward) sweep of the detuning. Since the ACZ force is “on” during a frequency ramp, the addition of an ARP sweep increases the impulse imparted to the atoms by 5% for  $\delta_{exp} = 0$  to 20% at  $\delta_{exp} = \pm 13$  MHz.

The Fig. 2(b) plot shows our ACZ force measurements as a function of  $\delta$  for 3 W of  $\mu\text{w}$  power and  $B_{dc} = 5.1$  G. The left axis shows the vertical displacement  $\Delta y$  produced by the ACZ impulse. In the no-ARP case, the ACZ force is proportional to  $\Delta y$  and is indicated on the right axis. This proportionality (and the right axis) is only approximately correct for ARP-based measurements because of the applied force during the ARP sweep. The “2-level theory” curves (see Appendix) use Eq. 1 to plot the expected  $\Delta y$  including the ARP sweep and employs no free parameters. The theory curve uses  $\Omega = 2\pi \times 1.284(22)$  MHz and  $d\Omega/dy = 2\pi \times 12.0(2.3)$  kHz/ $\mu\text{m}$ , which are inferred values for 3 W based on Rabi oscillations measurements with 30 mW of  $\mu\text{w}$  power. We note that if we assume a  $1/d$  dependence for  $B_{ac}$ , then this value for  $\Omega$  implies a  $\mu\text{w}$  current  $I_{ac} = 37$  mA rms. We determine  $d\Omega/dy$  from additional Rabi oscillation measurements 11  $\mu\text{m}$  below the standard ODT position. The  $\pm 19\%$  ( $1\sigma$ ) uncertainty in the prediction is shown by the colored bands. The 2-level theory agrees reasonably well with the data, though on-resonance (off-resonance) the force is a little larger (smaller) than expected. A two parameter fit removes the discrepancy between theory and data by reducing  $\Omega$  and increasing  $d\Omega/dy$  each by 20% from their measured values.

Fig. 2(c) shows the fraction of the atoms in  $|e\rangle$  vs.  $\delta$  for the Fig. 2(b) data. We integrate the absorption images used for the Fig. 2(b) data to obtain the atom number in  $|e\rangle$  for both the ARP and no-ARP cases. Control images with no  $\mu\text{w}$  pulse and thus with all atoms  $|e\rangle$ , taken immediately before and after the Fig. 2(b) data run, are used to determine the average total number of atoms  $N_{control}$ . The  $\mu\text{w}$  turn-off time is a little under 20 ns and negligibly affects the atomic populations. The “2-level theory” curves (see Appendix) assume an instantaneous  $\mu\text{w}$  turn-off and show the expected fraction of atoms in  $|e\rangle$ :  $|\langle e|\pm\rangle|^2$ . The 2-level theory matches the data, though ARP sweeps through resonance show some deviation. Taken together, figures 2(b) and 2(c) highlight that near resonance the ACZ force is strong but at the cost of mixing the  $|g\rangle$  and  $|e\rangle$  states. Off resonance, the ACZ force is reduced, but the  $|g\rangle$  and  $|e\rangle$  states experience much less mixing. In fact, the ACZ potential falls off as  $\hbar|\Omega|^2/4\delta$ , while the fractional population mixing falls off faster with detuning as  $|\Omega/2\delta|^2$ , similar to the AC Stark effect in optical dipole traps.

#### IV. TIME EVOLUTION

Next, we study the long-term time-evolution of the  $|\pm\rangle$  ACZ eigenstates with an eye towards future applications of ACZ potentials, such as trapping and spin-dependent positioning of atoms. Specifically, we determine the extent to which  $|\pm\rangle$  atoms (in ODT) acquire a  $|\mp\rangle$  component over time, whether from single-particle physics or collisions. However, due to rapid loss for atoms prepared in  $|+\rangle$  (with  $\delta \lesssim 0$ ), we focus primarily on the stability of atoms initially in  $|-\rangle$  (with  $\delta \gtrsim 0$ ), which evolve more slowly. We do not have an explanation for this difference in behavior between the two states, but it appears to be due to single particle physics, as we do not observe a change in the atom loss rate with collision rate.

We use a weak ACZ force produced by 20 mW of  $\mu\text{w}$  power to limit spin-dependent evaporation from the ODT:  $F_{ac}(\delta = 0)$  and  $\Omega$  in Fig. 2(b) are reduced by a factor of 13, resulting in a spin-dependent variation in trap depth of  $\pm 9\%$  for the  $|\mp\rangle$  states. Fig. 3(a) shows the experimental timing sequence. We transfer atoms in  $|e\rangle$  to  $|-\rangle$  with a 20 ms ARP sweep (ARP1) and then keep the  $\mu\text{w}$  power and  $\delta$  fixed for a variable hold time, during which atoms may evolve a  $|+\rangle$  component. A reverse ARP sweep (ARP2) maps the  $|-\rangle$  ( $|+\rangle$ ) component onto  $|e\rangle$  ( $|g\rangle$ ). The 1.5 ms long ARP3 sweep transfers atoms in  $|g\rangle$  to the  $|2, 0\rangle$  state. The ODT is then turned off, followed by a brief DC Stern Gerlach pulse, and a 0.1 ms laser “pre-pulse” to optically pump all of the atoms to  $|2, 2\rangle$  before the formal absorption imaging probe pulse. We measure the fraction of atoms in  $|-\rangle$ ,  $\eta = N_e/(N_g + N_e)$ , by simultaneously imaging the  $|e\rangle$  and  $|g\rangle$  populations  $N_e$  and  $N_g$ .

Fig. 3(b) shows the  $\delta = 0$  time evolution of  $\eta$  at several  $B_{dc}$  for atoms initially in  $|-\rangle$ . We take an empirical approach and find that the data can be approximately described by an initial exponential-like fast decay (amplitude  $A$  and decay time  $\tau$ ) from  $\eta \simeq 1$  to  $\eta = \eta_f$ , followed by a much slower decay, which is roughly linear out to 2 s (slope  $-\beta$ ). During the initial fast decay, we observe transfer of atoms between the two eigenstates, but with little atom loss from the ODT. In contrast, the slower decay described by  $\beta$  is characterized by spin-dependent atom loss from the ODT. We model the data with the following function:

$$\eta(t) = \eta_f + Ae^{-t/\tau} - \beta t \quad (2)$$

This equation describes the observed behavior reasonably well, but with clear deviations in some cases. For instance, the initial decay can feature momentary increases as seen in Fig. 3(b) at 39 G. The most reliable behavior is the settling of  $\eta$  to  $\eta_f$  after the initial decay, which we explore further. Fig. 4(a) summarizes the behavior of  $\eta_f$  with magnetic field (at  $\delta = 0$ ) and shows that atoms tend to stay in  $|-\rangle$  for large  $B_{dc}$ , while fields below 26 G lead to equal populations in the two eigenstates. The detuning dependence of  $\eta_f$  also varies with  $B_{dc}$ : Fig. 4(c) shows that  $\eta_f$  decreases significantly for  $\delta \lesssim 0.4$  MHz,

but that for large  $B_{dc}$  the decrease is less pronounced and occurs for  $\delta \lesssim 0$  MHz.

Finally, we find that  $\eta(t)$  does not depend on density. At 52 G with  $|-\rangle$  atoms at  $t = 2$  s, we measure  $\eta_f = 0.90(1)$  and  $0.91(2)$  for densities of  $9.6 \times 10^{12} \text{ cm}^{-3}$  and  $7.5 \times 10^{12} \text{ cm}^{-3}$  (collision rate  $k = 35, 22$  Hz), respectively. Likewise, the evolution of  $\eta$  for atoms initially in  $|+\rangle$  in Fig. 3(d) does not depend on collision rate. These null-results imply that the observed evolution is due to single particle physics, rather than collisions. We obtain a shorter  $\tau$  when the  $\mu\text{w}$  linewidth is increased at low  $B_{dc}$  with  $\delta = 0$ , indicating that detuning jitter (e.g. from  $\omega_{ac}$  or  $B_{dc}$ ) may contribute to the eigenstate evolution at short times. We do not have a model to explain the observed mixing of the eigenstates documented in Fig. 3 and Fig. 4. However, since the on-resonance splitting of the dressed atom eigenstates is  $\Omega = 2\pi \times 105$  kHz (at 20 mW of  $\mu\text{w}$  power), we speculate that detuning noise at this frequency or at odd-subharmonics [22, 23] could drive transitions between the eigenstates, thus accounting for the fast decay to  $\eta_f$ . An avenue for future study of the eigenstate mixing is to use a spatially flat  $\mu\text{w}$  field, so that  $\Omega$  can be varied to determine its role, but without risk of spin-dependent evaporation from the ODT.

We have also made an initial study of the time evolution of atoms prepared in  $|+\rangle$  and find that its short term behavior features a sharp “knee” that initiates the decay, at approximately 55 ms in Fig. 3(d) plot of  $\eta(t)$  for  $|+\rangle$  at 52 G. Its long term evolution shares the general features of the  $|-\rangle$  case decay:  $\eta_f$  is larger for increasing magnetic field  $B_{dc}$ , as well as increasing detuning  $\delta$ , and shows no density dependence. However, the  $|+\rangle$  data is noisier due to qualitatively faster trap losses and heating, thus limiting the reliable extraction of fit parameters. Furthermore, the sharp “knee” (at which point the decay begins), is unexplained and is a subject for further investigation. This behavior suggests a possible technical issue, but we have been unable to determine its cause.

## V. SPIN-SPECIFIC FORCE

A useful feature of the ACZ force is the ability to target a specific spin-state transition pair while leaving other states largely unaffected. In Fig. 5(a), we release atoms in a spin mixture of  $|2, 2\rangle$ ,  $|2, 1\rangle$ , and  $|2, 0\rangle$  states from the ODT, briefly apply a resonant ACZ force to one of the states, and then use a magnetic gradient pulse to separate the states horizontally (Stern-Gerlach effect) before imaging. An ACZ push targeted to the  $|2, 2\rangle$  state using the  $|e\rangle \leftrightarrow |g\rangle$  transition is shown in Fig. 5(a1). In Fig. 5(a3), we apply an ACZ pull to the  $|2, 1\rangle$  state using the  $|2, 1\rangle \leftrightarrow |1, 0\rangle$  transition [24]. For reference, the case of no ACZ force is shown in Fig. 5(a2). Alternatively, if the ACZ force is applied while the spin mixture is in the ODT, then we can selectively eject atoms of a given spin by pushing them out of the trap. Fig. 5(b) shows the selective removal of the  $|2, 2\rangle$ ,  $|2, 1\rangle$ , and  $|2, 0\rangle$  states from

the ODT before Stern-Gerlach imaging.

The ACZ force can also be applied to atoms in magnetically insensitive spin-states, such as  $|2, 0\rangle$ , which are of metrological interest. Fig. 5(c) shows the application of an ACZ force to untrapped atoms in  $|2, 0\rangle$ . In contrast with the rest of this work, this ACZ force uses the  $\pi$  transition  $|2, 0\rangle \leftrightarrow |1, 0\rangle$  with  $B_{dc}$  oriented along the  $x$ -axis. The matrix element for this transition is somewhat larger than for the  $|e\rangle \leftrightarrow |g\rangle$  transition, which results in a 15% stronger ACZ force. The higher initial temperature of the atoms and larger cloud size contribute to the curved distortion of the pushed and pulled clouds. This scheme was also used in Fig. 5(b2) and Fig. 5(b3) by employing the  $|2, 1\rangle \leftrightarrow |1, 1\rangle$  and  $|2, 0\rangle \leftrightarrow |1, 0\rangle$  transitions, respectively.

## VI. CONCLUSION

In conclusion, we have measured the ACZ force produced by a  $\mu\text{w}$  near-field from an atom chip and found agreement with 2-level dressed atom theory [15]. The force is resonant and bipolar and can be targeted to a specific spin-state. At 100  $\mu\text{m}$  with a 3 W amplifier, the  $\sim 3\text{mg}$  force is sufficient for practical manipulations of ultracold atoms. Larger forces should be possible with improved  $\mu\text{w}$  impedance matching to the atom chip, higher  $\mu\text{w}$  power, or a shorter chip-atom distance. Our initial study on the continuous application of a  $\mu\text{w}$  near-field shows that the long-term eigenstate stability improves with larger DC magnetic field and  $\mu\text{w}$  detuning. We note that we have also pushed atoms in a micro-magnetic chip trap with a far off-resonance ACZ force (see also [17]) with little loss. ACZ potentials are well suited for spin or species specific spatial manipulation applications. For example, an ACZ force could enable sympathetic cooling in an ODT by selectively evaporating one atomic spin state or species within a mixture [25]. Alternatively, an ACZ force could be used for spin-dependent beamsplitting (see Fig. 2(a)) and interferometry [17]. Finally, a local minimum in a  $\mu\text{w}$  near-field could provide spin or species-specific trapping [26, 27].

## ACKNOWLEDGMENTS

This work was supported by AFOSR and the College of William and Mary. C. T. F. and A. J. P. acknowledge additional support from the Virginia Space Grant Consortium. We thank C. Sukenik (Old Dominion U.) for the long-term loan of the laser used for the optical trap. We thank I. Spielman for helpful discussion at the start of this work.

## APPENDIX

The black “2-level theory” curves in Fig. 2(b) give the variation in vertical position  $\Delta y$  of the atoms due to the applied AC Zeeman impulse. The curves include the contribution to the atom’s impulse by the  $t_{ARP} = 0.1$  ms ARP sweep and the  $t_{\mu w} = 0.5$  ms fixed detuning portion of the  $\mu w$  pulse. The impulse from the ARP sweep is calculated by inserting a linear ramp  $\delta(t) = \delta_0 + (\delta - \delta_0)t/t_{ARP}$  and then integrating Eq. 1 with respect to time from  $t = 0$  to  $t = t_{ARP}$ . The impulse at fixed detuning is given by  $F_{ac}t_{\mu w}$ . The travel distance  $\Delta y$  (vertical) due to the impulse is obtained by multiplying the impulse by the time of flight  $\Delta t$  and dividing by the mass  $m$  of the atom:

$$\begin{aligned} \Delta y_{\pm} &= \Delta y_{ARP} + \Delta y_{\mu w} \\ &= \pm \frac{\hbar}{2} \Omega \frac{d\Omega}{dr} \frac{\Delta t}{m} \left\{ \frac{t_{ARP}}{\delta - \delta_0} \ln \left( \frac{\delta + \sqrt{\Omega^2 + \delta^2}}{\delta_0 + \sqrt{\Omega^2 + \delta_0^2}} \right) + \frac{t_{\mu w}}{\sqrt{\Omega^2 + \delta^2}} \right\} \end{aligned} \quad (\text{A.1})$$

The black “2-level theory” curves in Fig. 2(c) give the fraction of atoms in the  $|e\rangle$  state for the AC Zeeman impulse measurements in Fig. 2(b). In the measurements with an ARP-sweep, the atoms are placed in either the  $|+\rangle$  or  $|-\rangle$  eigenstate, and the probability to find an atom in  $|e\rangle$  is given by [15]

$$P(e|+) = |\langle e|+\rangle|^2 = (\Omega' - \delta)^2/\xi^2 \quad (\text{A.2})$$

$$P(e|-) = |\langle e|-\rangle|^2 = \Omega^2/\xi^2 \quad (\text{A.3})$$

with  $\Omega' = \sqrt{\delta^2 + \Omega^2}$  and  $\xi = \sqrt{\Omega^2 + (\Omega' - \delta)^2}$ . In the case of the “no-ARP” measurements, we measure the fraction of atoms in  $|e\rangle$  that have been pushed down from the chip, and thus projected onto the  $|+\rangle$  state with probability  $P(+|e) = |\langle +|e\rangle|^2$  given by Eq. A.2. The fraction of atoms in  $|e\rangle$  that have been pulled up towards the chip have been projected onto the  $|-\rangle$  state with probability  $P(-|e) = |\langle -|e\rangle|^2$  given by Eq. A.3.

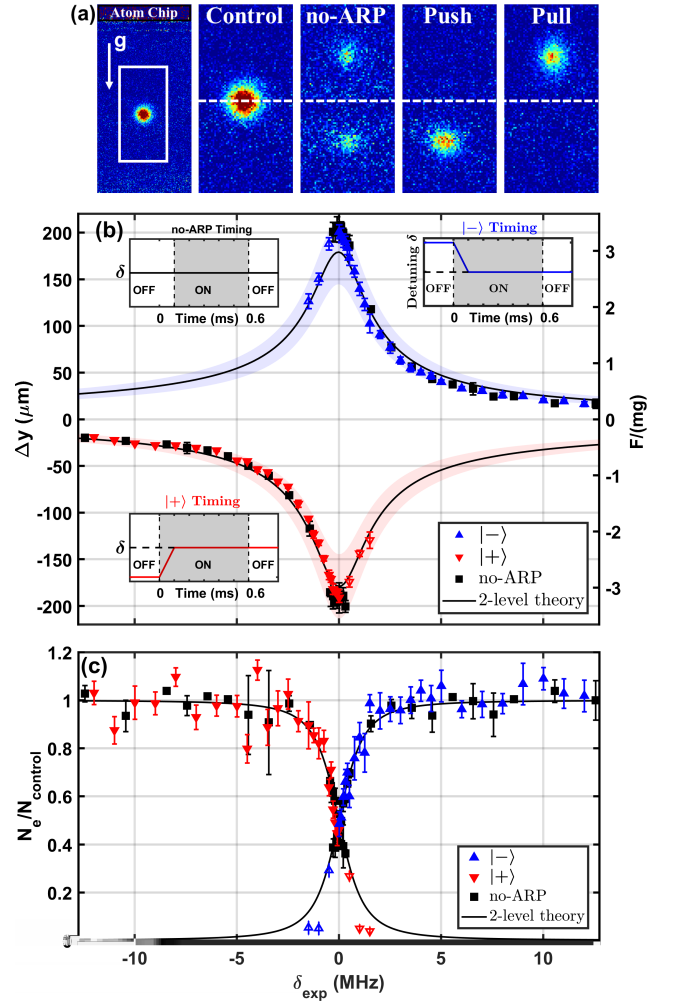


FIG. 2. AC Zeeman force measurement. (a) Sample of false color absorption images used in (b,c). Atom Chip:  $\mu w$  off and zoom-in box for other images. Control:  $\mu w$  off. no-ARP, Push, and Pull: resonant  $\mu w$  pulse ( $\delta = 0$ ) with atoms in  $|e\rangle$ ,  $|+\rangle$ , and  $|-\rangle$ , respectively. (b) Atom cloud displacement  $\Delta y$  vs.  $\mu w$  detuning  $\delta$  with an ARP sweep to constrain atoms to the  $|\pm\rangle$  eigenstates (triangles) and with no sweep (no-ARP, squares). The right axis is the ACZ force for the no-ARP case and is approximately correct for  $|\pm\rangle$  data. The black curves are not fits but predictions ( $\pm 1\sigma$  shading) for  $\Delta y$  based on Eq. 1 and independently measured values for  $\Omega$  and  $d\Omega/dy$ , including the impulse generated from the ARP sweep. *Insets*: detuning vs. time during the  $\mu w$  pulse (ON) for the “no-ARP”,  $|+\rangle$ , and  $|-\rangle$  state preparation cases. (c) Atom number in  $|e\rangle$  vs.  $\delta$  relative to control data without a  $\mu w$  pulse. The black curves are predictions [15] using the independently measured value for  $\Omega$  and assume an instantaneous turn-off time. Data points are averages of five measurements; error bars give the standard deviation of the mean. The six open triangles in (b,c) were analyzed differently due to low signal.

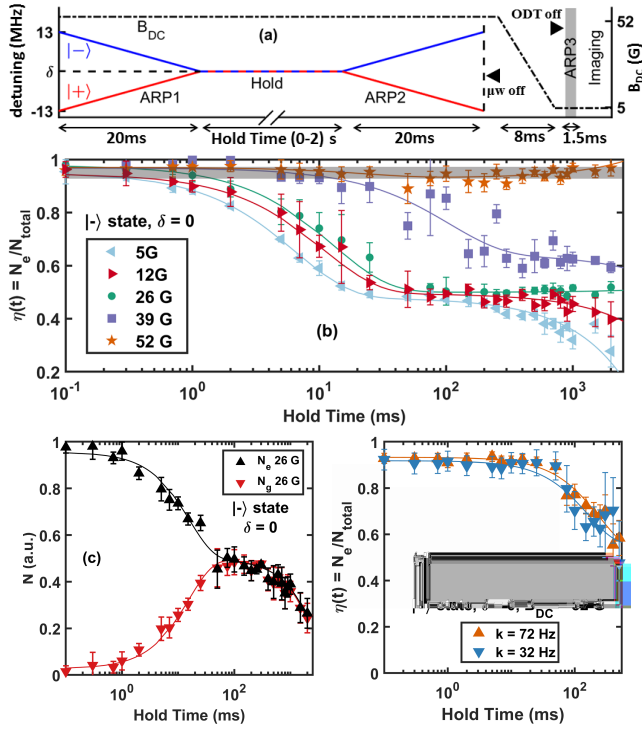


FIG. 3. Time evolution of the ACZ eigenstates. (a) Timing sequence showing the preparation of the  $|\pm\rangle$  states (ARP1), variable hold time  $t$ , mapping back to the  $|e\rangle$  and  $|g\rangle$  states (ARP2), and the transfer of atoms in  $|g\rangle$  to  $|2,0\rangle$  for imaging (ARP3). The right y-axis and dash-dot line shows an example of  $B_{dc}$  timing for  $B_{dc} = 52\text{G}$ . (b) Plot of the fraction of atoms in  $|-\rangle$ ,  $\eta(t)$ , versus  $t$  for different  $B_{dc}$  at  $\delta = 0$ . The grey band indicates the range of  $\eta(t)$  scatter for no microwaves. The solid lines represent fits using the Eq. 2 model. (c) Atom numbers  $N_e$  and  $N_g$  in  $|e\rangle$  and  $|g\rangle$ , respectively, versus  $t$  for  $B_{dc} = 26\text{G}$  and  $\delta = 0$ . (d) Plot of  $\eta(t)$  in the  $|+\rangle$  case at two different collision rates  $k$  with  $\delta = 0$  and  $B_{dc} = 52\text{G}$ . The time axes are plotted on a log scale for (b-d) to highlight the difference between the exponential and linear decays.

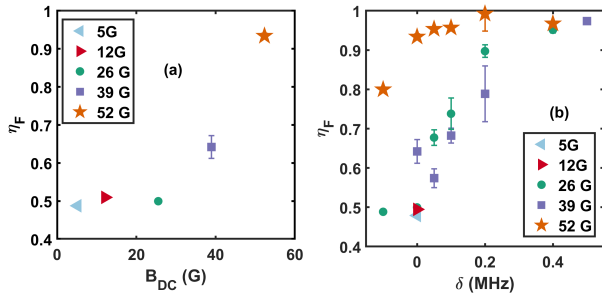


FIG. 4. Behavior of  $\eta_f$  with magnetic field and detuning extracted from fitting  $\eta(t)$  data to Eq. 2. (a) Plot of  $\eta_f$ , the short-term decay floor for  $\eta$ , versus  $B_{dc}$  for  $\delta = 0$ . (b) Plot of  $\eta_f$  versus  $\mu\text{w}$  detuning  $\delta$  for different  $B_{dc}$ .

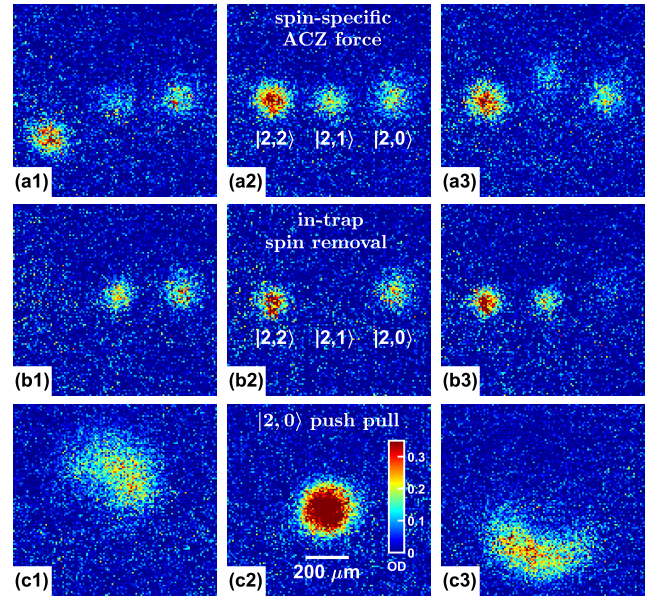


FIG. 5. Demonstrations of spin selectivity. (a) Spin-specific targeting of the ACZ force to an untrapped spin-mixture using the procedure and orientation of Fig. 2(b). A 0.5 ms ACZ impulse (a1) pushes down  $|2,2\rangle$ , (a2) is off, and (a3) pulls up  $|2,1\rangle$ . The spins are separated horizontally after the ACZ force is applied. (b) Targeted removal of spin states from a spin mixture in the ODT with  $F_{ACZ} \simeq 3mg\hat{y}$  applied for 5 ms. (c) The ACZ force applied to atoms in  $|2,0\rangle$ : a 0.5 ms impulse (c1) pulls up, (c2) is off, and (c3) pushes down. All the false color images share the same length scale and optical depth color scale, given in (c2). In all frames, the ACZ force is applied with 3 W of  $\mu\text{w}$  power and  $\delta = 0$ . We use  $B_{dc} = 52\text{G}$  along the  $z$ -axis for frames (a1-a3) and (b1), and  $B_{dc} = 46\text{G}$  along the  $x$ -axis for frames (b2-b3) and (c1-c3).

- 
- [1] N. F. Ramsey, *Phys. Rev.* **78**, 695 (1950).
- [2] R. Wynands and S. Weyers, *Metrologia* **42**, S64 (2005).
- [3] S. Bize, P. Laurent, M. Abgrall, H. Marion, I. Maksimovic, L. Cacciapuoti, J. Grünert, C. Vian, F. Pereira dos Santos, P. Rosenbusch, P. Lemonde, G. Santarelli, P. Wolf, A. Clairon, A. Luiten, M. Tobar, and C. Salomon, *J. Phys. B: At. Mol. Opt. Phys.* **38**, S449 (2005).
- [4] A. D. Ludlow, M. M. Boyd, J. Ye, E. Peik, and P. O. Schmidt, *Rev. Mod. Phys.* **87**, 637 (2015).
- [5] W. Happer, *Rev. Mod. Phys.* **44**, 169 (1972).
- [6] H. F. Hess, G. P. Kochanski, J. M. Doyle, N. Masuhara, D. Kleppner, and T. J. Greytak, *Phys. Rev. Lett.* **59**, 672 (1987).
- [7] H. J. Metcalf and P. van der Straten, *Laser Cooling and Trapping* (Springer, 1999).
- [8] W. Ketterle, D. S. Durfee, and D. M. Stamper-Kurn, in *Proc. Int. Sch. Phys. Enrico Fermi* (IOS Press, Amsterdam, 1999) pp. 67–176.
- [9] N. Lundblad, M. Schlosser, and J. V. Porto, *Phys. Rev. A* **81**, 031611 (2010).
- [10] C. Y. Park, J. Kim, J. M. Song, and D. Cho, *Phys. Rev. A* **65**, 033410 (2002).
- [11] O. Mandel, M. Greiner, A. Widera, T. Rom, T. W. Hänsch, and I. Bloch, *Phys. Rev. Lett.* **91**, 010407 (2003).
- [12] M. Bloom and K. Erdman, *Can. J. Phys.* **40**, 179 (1962).
- [13] M. Bloom, E. Enga, and H. Lew, *Can. J. Phys.* **45**, 1481 (1967).
- [14] S. R. Leslie, J. Guzman, M. Vengalattore, J. D. Sau, M. L. Cohen, and D. M. Stamper-Kurn, *Phys. Rev. A* **79**, 043631 (2009).
- [15] C. C. Agosta, I. F. Silvera, H. T. C. Stoof, and B. J. Verhaar, *Phys. Rev. Lett.* **62**, 2361 (1989).
- [16] R. J. C. Spreeuw, C. Gerz, L. S. Goldner, W. D. Phillips, S. L. Rolston, C. I. Westbrook, M. W. Reynolds, and I. F. Silvera, *Phys. Rev. Lett.* **72**, 3162 (1994).
- [17] P. Böhi, M. F. Riedel, J. Hoffrogge, J. Reichel, T. W. Hänsch, and P. Treutlein, *Nat. Phys.* **5**, 592 (2009).
- [18] C. Ospelkaus, U. Warring, Y. Colombe, K. R. Brown, J. M. Amini, D. Leibfried, and D. J. Wineland, *Nature* **476**, 181 (2011).
- [19] T. P. Harty, D. T. C. Allcock, C. J. Ballance, L. Guidoni, H. A. Janacek, N. M. Linke, D. N. Stacey, and D. M. Lucas, *Phys. Rev. Lett.* **113**, 220501 (2014).
- [20] T. Schumm, S. Hofferberth, L. M. Andersson, S. Wildermuth, S. Groth, I. Bar-Joseph, J. Schmiedmayer, and P. Krüger, *Nat. Phys.* **1**, 57 (2005).
- [21] M. K. Ivory, A. R. Ziltz, C. T. Fancher, A. J. Pyle, A. Sensharma, B. Chase, J. P. Field, A. Garcia, D. Jervis, and S. Aubin, *Rev. Sci. Instrum.* **85**, 043102 (2014).
- [22] R. J. C. Spreeuw and J. Woerdman, in *Prog. Opt.* (1993) Chap. V, pp. 263–319.
- [23] R. Graham and M. Höhnerbach, *Phys. Lett. A* **101**, 61 (1984).
- [24] The  $|2, 0\rangle$  state is pulled slightly in Fig. 4(a3), due to the quasi-degeneracy of the  $|2, 1\rangle \leftrightarrow |1, 0\rangle$  transition and weaker  $|2, 0\rangle \leftrightarrow |1, 1\rangle$  transition.
- [25] M. Brown-Hayes, Q. Wei, C. Presilla, and R. Onofrio, *Phys. Rev. A* **78**, 013617 (2008).
- [26] L. J. LeBlanc and J. H. Thywissen, *Phys. Rev. A* **75**, 053612 (2007).
- [27] J. Catani, G. Barontini, G. Lamporesi, F. Rabatti, G. Thalhammer, F. Minardi, S. Stringari, and M. Inguscio, *Phys. Rev. Lett.* **103**, 140401 (2009).